Multiscale simulation of high-order harmonic generation: From microscopic to macroscopic

Xiao-Min Tong ⬤[*]

Center for Computational Sciences, University of Tsukuba, 1-1-1 Tennodai, Tsukuba, Ibaraki 305-8573, Japan

We developed a theoretical method to study the high-order harmonic generation (HHG) from a gas target in an intense laser pulse. We obtain the microscopic HHG by solving the time-dependent Schrödinger equation with a single-active-electron approximation and the macroscopic HHG by summing over all the microscopic HHG with phase matching and self-absorption in two scales. One is in the laser wavelength scale, within which the laser peak intensity does not change while the propagation phase changes. Another is in the laser beam waist scale, within which the laser intensity and Gouy phase shift change. Taking the Ar atom as an example, we calculate the macroscopic HHG energy distribution and divergence. We also discuss the dependency of the macroscopic HHG on the gas pressure and gas jet position.

I. INTRODUCTION

High-order harmonic generation (HHG), discovered in the later 1980s [1], provides a way to generate a desktop x-ray laser. The HHG has been studied extensively, from an attosecond pulse train to a single attosecond pulse in the time domain [2,3] and several tens of eV to several keV in the energy domain [4,5]. The HHG can be controlled by two-color pulses using linearly [6,7] or circularly polarized laser fields [8]. Since the discovery of the vertex laser field or twisted laser pulse [9–13], one can control the polarization and spatial distribution of the HHG in the far field [14]. The HHG, or attosecond pulses, can be used to probe electron dynamics in femtosecond and even attosecond time scales [15–20].

To calculate the macroscopic HHG, one needs the microscopic HHG from individual atoms and the macroscopic parameters, like laser intensity distribution and gas pressure. The microscopic HHG, the single atomic response, can be calculated by solving the time-dependent Schrödinger equation (TDSE). Directly solving the TDSE for a many-electron system is formidable work even for a supercomputer. The best available method so far is the time-dependent density-functional theory (TDDFT) [21], which considers the electron-electron dynamical correlations [22–26]. The TDDFT can be used to study the properties of the microscopic HHG for a given laser pulse. It is difficult to use the method for a macroscopic simulation since too many laser parameters are involved.

Alternatively, the strong-field approximation (SFA) [27] provides a simple way to estimate the microscopic HHG. With the SFA, the electron parent-core interaction is ignored and the electron wave function is described by an analytical Volkov wave function [28]. With the analytical Volkov wave function, the simulation is simplified greatly. The SFA can be improved by using the Coulomb-Volkov wave function [29],

in which the electron parent-core interaction is approximated by a Coulomb interaction. The method is popularly used for atomic above-the-threshold ionization [30,31]. Recently, the partial-wave representation of the SFA method [32,33] has been employed to include a better electron parent-core interaction beyond the Coulomb interaction. The method can also be applied to the HHG process. Based on the three-step model [34], the last step, the radiative recombination, can be further improved based on the quantitative rescattering theory [35]. The HHG is emitted through a coherent process and the relative phases play an important role. The SFA method relies on the classical trajectories to get the phase or simply neglect part of them [36]. For a single atom response, the Coulomb phase could play an important role as shown in Ref. [37], which is neglected in the SFA.

The atomic HHG can be calculated by solving the TDSE [38] with the single-active-electron (SAE) approximation. With a proper model potential, such a single-electron-like simulation can provide all the HHG information, including the phase at a single atom level. The method is affordable computationally with the quantum phase information.

In principle, the macroscopic HHG is obtained by summing all the atomic dipoles with the proper propagation phase and laser intensity spatial distribution. Directly summing all the atomic dipoles is impossible since the atomic and macroscopic scales differ in several orders. One way is to use the discrete dipole approximation [39,40]. Even in such a case, one still needs the microscopic HHG at many laser intensities due to beam spatial distribution. Therefore, to calculate the macroscopic HHG [12,40,41], in most cases, one has to estimate the microscopic HHG.

Here we propose a procedure to calculate the macroscopic HHG. We first calculate the atomic HHG in a broad laser intensity range by solving the TDSE with an SAE approximation, in which the phases associated with the atomic HHG are considered. Using this as a database, we take into account the propagation effect or phase matching in a multiscale simulation. A fine grid with grid space is in the order of the
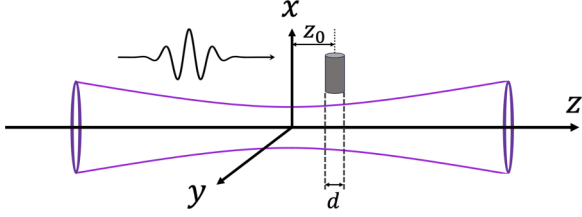
_____
[*]tong.xiaomin.ga@u.tsukuba.ac.jp

FIG. 1. Setup of the coordinate system, gas jet position, and gas thickness for macroscopic simulation, which mimics the experimental setup.

wavelength, and a coarse grid with grid space is in the order of the laser beam waist, which is much larger than the wavelength [42]. We will detail the formulas used in the simulation and physical reasons for the choice in Sec. II, followed by a discussion on the dependence of the macroscopic HHG on the laser beam spatial distribution, gas density, and gas jet position in Sec. III.

II. THEORETICAL METHOD

To generate HHG, one needs a laser beam and a working material, atoms. Therefore, we first describe the laser beam, then the atomic dipole generated in a strong field, and finally the macroscopic HHG including the phase matching.

A. Laser beam

With the development of optical technology, optical vertices or twisted laser beams have been available in laboratories. The spatial distribution of the beam can be described by a Laguerre-Gaussian (LG) function in a cylindrical coordinate as shown in Fig. 1. Here we assume that the laser propagates along the z direction with focal point at the origin. The general expression of the LG laser electric field [10,13,43,44] at a position $r = (z, r, \phi)$ is

$$\boldsymbol{E}(\boldsymbol{r}) = \boldsymbol{E}_0 S(r, z) e^{i\Psi_{\mathrm{IR}}(r,z)+il\varphi}, \tag{1}$$

with

$$S(r, z) = \frac{W_0}{W(z)} \left(\frac{\sqrt{2}r}{W(z)}\right)^{|l|} L_p^{|l|}\left[\frac{2r^2}{W^2(z)}\right] e^{-\frac{r^2}{W^2(z)}}, \tag{2a}$$

$$\Phi_{\mathrm{IR}}(r, z) = k\frac{r^2}{2R(z)} + \Psi_G(z). \tag{2b}$$

Here l is the orbital angular momentum (OAM) of the LG beam [11], p is the number of nodes in the radial direction, and $\boldsymbol{E}_0$ and W_0 are the electric-field vector and laser beam waist. $L_p^{|l|}[x]$ is an associated Laguerre polynomial. We choose the focal point as the origin and omit a factor used in Ref. [43]. Defining the Rayleigh range by the laser wavelength λ as

$$z_r = \pi\frac{W_0^2}{\lambda}, $$

the quantities in Eq. (2) are expressed as

$$W(z) = W_0\sqrt{1 + z^2/z_r^2}, \tag{3a}$$

$$R(z) = \frac{z^2 + z_r^2}{z}, \tag{3b}$$

$$\Phi_G(z) = -(|l| + 2p + 1)\arctan\left(\frac{z}{z_r}\right). \tag{3c}$$

The laser intensity in Eq. (2a) changes over the space in the order of W_0, so as the IR laser phase in Eq. (2b). Including the time propagation, the time-dependent local electric field at r is written as

$$\boldsymbol{E}(\boldsymbol{r}, t) = \boldsymbol{E}_0 S(r, z) \tag{4a}$$

$$\times e^{i\Psi_{\mathrm{IR}}(r,z)+il\varphi} \tag{4b}$$

$$\times e^{ikz-i\omega_0 t} f\left(t - \frac{z}{v}\right), \tag{4c}$$

with v the velocity of light in the media and $f(t)$ the laser pulse envelope. k and ω_0 are the laser wave number and frequency, respectively. The above equation is valid for a long pulse which is the case of the present paper. For a short or single-cycle pulse, the intensity space distribution depends on the wavelength and we have to rewrite Eq. (4).

Three terms in Eq. (4) change differently in the different scales. The local electric field in Eq. (4c) oscillates as a function of time, while it does not change in space if we consider the retardation time $\tilde{t} = t - z/v$. The position dependent peak strength in Eq. (4a) and phase in Eq. (4b) change over the space in the order of the beam waist, which is orders larger [42] than the laser wavelength. The phase in Eq. (4b) is the sum of the phase given in Eq. (2b) and the phase of OAM, which can be treated analytically as shown in Eq. (17). We also have to consider the phase associated with the laser and HHG propagation, which is in the order of the laser wavelength. Therefore, we calculate the macroscopic HHG from three spatial scales: (1) atomic scale, in which we assume that the laser peak strength is a constant and we calculate the atomic HHG in dipole approximation without the propagation effect; (2) wavelength scale, in which we consider the laser and HHG propagation effect while assuming that the laser peak intensity and IR laser phase do not change; and (3) laser beam waist scale, in which we consider the macroscopic HHG emitted from different coarse grids including both laser peak intensities and propagation effects. Although we discussed the LG beam, which is popularly used in strong fields, the idea works for other types of beam so long as we know the space and time-dependent electric field as shown in Eq. (4).

B. Microscopic HHG

The dynamics of atoms in a strong field can be studied by solving the TDSE as (atomic units $m_e = \hbar = e = 1$ are used throughout unless stated otherwise)

$$i\frac{\partial}{\partial t}\psi(t) = H(t)\psi(t), \tag{5}$$

with

$$H(t) = -\frac{\nabla^2}{2} + V(r) - \boldsymbol{r} \cdot \boldsymbol{E}(t). \tag{6}$$

The first term on the right-hand side of Eq. (6) is the kinetic operator, the second term represents the electron parent-core interaction, and the last term stands for the electron-laser interaction with the dipole approximation. The electron parent-core interaction is described by a model potential

[45]. The equation is solved by a second-order split-operator method with a generalized pseudospectral grid in differential form [38]. Equation (5) can be solved in integral form [46] as

$$\psi(t) = i \int_0^t e^{-i \int_{t'}^{\infty} H(t'')dt''} \mathbf{r} \cdot \mathbf{E}(t') e^{-i\epsilon_g t'} \psi_g dt'$$
$$+ e^{-i\epsilon_g t} \psi_g, \qquad (7)$$

for a laser pulse from time $t = 0$ to ∞. Here ψ_g is the ground-state wave function and ϵ_g is the corresponding orbital energy. The advantage of the integral form is that the Hamiltonian $H(t)$ in the time propagation can be different from the Hamiltonian of the ground state. Therefore, we can calculate the atomic HHG under the SFA by setting $V(r) = 0$ in $H(t)$. We can also add the Coulomb correction to the SFA (denoted by SFAc) by setting $V(r) = -1/r$ and removing all the bound states. Equation (7) essentially is the same as the partial-wave representation of the SFA [32] in physics, but treated in different numerical methods if we use the same model potential. With the time-dependent wave function, the time-dependent induced dipole is calculated as

$$\mathbf{d}(t) = \langle \psi(t) | \hat{d} | \psi(t) \rangle, \qquad (8)$$

with $\hat{d}$ the dipole operator, which can be in length, velocity, or acceleration forms [47,48]. The Fourier transform of the induced dipole, $\mathbf{d}(\omega)$, provides the local atomic dipole at space $\mathbf{r}$ as $\mathbf{d}_{\text{atm}}(\mathbf{r}, \omega)$ and it contains all the phases at a single-atom level. The single-atom dipoles at different spaces correspond to the different peak intensities with the same laser pulse and center frequency. All the dipoles can be calculated in parallel with a many-core workstation or many-node supercomputer. Note that in the atomic HHG simulation, we only consider laser intensities and time-dependent parts in Eq. (4c) without the phase factor in Eq. (4b).

C. Macroscopic HHG

Additionally, the position dependent phase of the laser field $\Psi_{\text{IR}}(r, z) + l\varphi$ multiplied by the harmonic order should be added to the local atomic dipole. Thus, using the local electric field in Eq. (4), the microscopic dipole is written as

$$\mathbf{d}(\mathbf{r}, \omega) = \mathbf{d}_{\text{atm}}(\mathbf{r}, \omega) e^{i\Psi_{\text{IR}}(r,z)\omega/\omega_0 + i[\omega/\omega_0]l\varphi}. \qquad (9)$$

To calculate the macroscopic HHG, we have to consider propagation. It takes time

$$t_1 = \frac{1}{c} \int_{z_a}^{z} n_0(\omega_0, z) dz$$

for the laser pulse to reach the position $\mathbf{r}$ and time

$$t_2 = \frac{1}{c} \int_z^{z_b} n(\omega, z) dz + \frac{|\mathbf{r}_d - \mathbf{r}_b|}{c}$$

for the HHG to reach the detector in the far field at $\mathbf{r}_d$. Here n_0 and n are the refractive indices of the media for the lights with frequencies of ω_0 and ω, respectively, and $\mathbf{r}_b$ is the right-hand-side boundary of the media. Here we account for the propagation phase from the left boundary of the media. The propagation results in a phase

$$\Psi_p(\mathbf{r}) = \frac{\omega}{\omega_0} k_0 (n_0 z + n|\mathbf{r} - \mathbf{r}_b| + |\mathbf{r}_d - \mathbf{r}_b|).$$

In a far-field approximation when $r_d \gg r$, $|\mathbf{r}_d - \mathbf{r}| \approx r_d - \hat{\mathbf{r}}_d \cdot \mathbf{r}$ and the phase is recast as

$$\Psi_p(\mathbf{r}) = \frac{\omega}{\omega_0} k_0 (n_0 z - n\hat{\mathbf{r}}_d \cdot \mathbf{r})$$
$$+ \frac{\omega}{\omega_0} k_0 [r_d + (n-1)\hat{\mathbf{r}}_d \cdot \mathbf{r}_b].$$

The last term is a constant and we remove the part and explicitly express the phase as

$$\Psi_p(\mathbf{r}) = \frac{\omega}{\omega_0} k_0 [(n_0 - n\cos\theta_d)z]$$
$$- \frac{\omega}{\omega_0} k_0 [r\sin\theta_d \cos(\varphi - \varphi_d)],$$

with (θ_d, φ_d) the direction of HHG in the far field. Assuming that the IR intensities centered at $\mathbf{r} = (r, \varphi, z)$ within dr, dz, and $d\varphi$ space are the same, the far-field HHG electric field from the dipole emitter $d\mathbf{D}(\mathbf{r}, \omega)$ is

$$d\mathbf{E}(\hat{\mathbf{r}}_d, \mathbf{r}, \omega) = \frac{1}{|\mathbf{r}_d - \mathbf{r}|} \{ \hat{\mathbf{r}}_d \times [\hat{\mathbf{r}}_d \times d\mathbf{D}(\mathbf{r}, \omega)] \}$$
$$\propto \{ \hat{\mathbf{r}}_d [\hat{\mathbf{r}}_d \cdot d\mathbf{D}(\mathbf{r}, \omega)] - d\mathbf{D}(\mathbf{r}, \omega) \}, \quad (10)$$

with $d\mathbf{D}(\mathbf{r}, \omega)$ the emitted dipole in the media within a volume of $r dr dz d\varphi$. To derive Eq. (10), we use the far-field approximation ($r_d \gg d$) and add the propagation phase onto $d\mathbf{D}(\mathbf{r}, \omega)$ in acceleration form. The total electric field in the far field in the $\hat{\mathbf{r}}$ direction is

$$\mathbf{E}(\hat{\mathbf{r}}_d, \omega) \propto \{ \hat{\mathbf{r}}_d [\hat{\mathbf{r}}_d \cdot \mathbf{D}(\hat{\mathbf{r}}_d, \omega)] - \mathbf{D}(\hat{\mathbf{r}}_d, \omega) \}, \qquad (11)$$

with $\mathbf{D}(\hat{\mathbf{r}}_d, \omega)$ written as

$$\mathbf{D}(\hat{\mathbf{r}}_d, \omega) = \int d\mathbf{D}(\mathbf{r}, \omega) = \int \mathbf{d}_{\text{atm}}(r, z, \omega) n_{\text{atm}}(r, z) \quad (12a)$$

$$\times e^{i\Psi_{\text{IR}}(r,z)\frac{\omega}{\omega_0}} e^{-\Gamma(\omega)(z_b - z)} \qquad (12b)$$

$$\times e^{i\Psi_p(\mathbf{r}) + i[\omega/\omega_0]l\varphi} r dr dz d\varphi, \qquad (12c)$$

with n_{atm} the gas density. All phase factors, like atomic dipole, laser phase including the OAM, and self-absorption, are included in Eq. (12).

The above equation connects the microscopic HHG to the observed macroscopic HHG. The macroscopic electric field in far field is the sum or integral of all the microscopic dipole emitters in Eq. (10). The sizes of microscopic and macroscopic differ in several orders. Now we look at the dipole field in Eqs. (12a)–(12c). The first two terms in Eq. (12) change over the space in the order of beam waist W_0, and the phase in Eq. (12c) changes over the space in the order of wavelength λ. Since $W_0 \gg \lambda$, we separate the above integral into two domains, a fine grid with the integration over a cell in a coarse grid.

In Eq. (12), we choose dr and dz in a fraction of the beam waist and sum over all the cells, and the macroscopic dipole is written as

$$\mathbf{D}(\hat{\mathbf{r}}_d, \omega) = \sum_{ij} \mathbf{d}_{\text{atm}}(r_i, z_j, \omega) n_{\text{atm}}(r_i, z_j) \qquad (13a)$$

$$\times e^{i\Psi_{\text{IR}}(r_i, z_j)\frac{\omega}{\omega_0}} e^{-\Gamma(\omega)(z_b - z_j)} \qquad (13b)$$

$$\times F_P(r_i, z_j, \theta_d, \omega), \qquad (13c)$$

with

$$F_P(r_i, z_j, \theta_d, \omega) = \int e^{i\Psi_p(\boldsymbol{r}) + i[\omega/\omega_0]l\varphi} r \, dr \, dz \, d\varphi. \quad (14)$$

F_P stands for the phase propagation within a Δr and Δz cell, and we call it the fine grid integration. $e^{-\Gamma(\omega)(z_b - z)}$ represents the self-absorption of the HHG by the media.

The phase in Eq. (14) is explicitly written as

$$\Psi_p(\boldsymbol{r}) + \left[\frac{\omega}{\omega_0}\right]l\varphi = \left(\frac{\omega}{\omega_0}k_0 z(n_0 - n\cos\theta_d)\right)$$
$$+ \left(\left[\frac{\omega}{\omega_0}\right]l\varphi - n\frac{\omega}{\omega_0}k_0 r \sin\theta_d \cos\varphi\right). \quad (15)$$

In Eq. (15), the phase in F_p is separated into two groups. One is only a function of z (the first term on the left-hand side of the equation), and another is a function of r and φ. Therefore the three-dimensional integral in Eq. (14) is recast as a product of one- and two-dimensional integrals as

$$F_P(r_i, z_j, \theta_d, \omega) = F_1(r_i, \theta_d, \omega) F_2(z_j, \theta_d, \omega). \quad (16)$$

We integrate over z from $z_j - \Delta z/2$ to $z_j + \Delta z/2$ as

$$F_1(z_j, \theta_d, \omega) = \int_{z_j - \Delta z/2}^{z + \Delta z/2} e^{i\frac{\omega}{\omega_0}k_0 z(n_0 - n\cos\theta_d)} dz$$
$$= \frac{\sin x \Delta z}{x} e^{i2xz_j}$$

with

$$x = \frac{\omega}{2\omega_0} k_0 (n_0 - n\cos\theta_d).$$

For the second term in Eq. (15), we first integrate over φ analytically as

$$F_J(r, \theta_d, \omega) = \int_0^{2\pi} e^{i\left[\frac{\omega}{\omega_0}\right]l\varphi - in\frac{\omega}{\omega_0}k_0 r \sin\theta_d \cos\varphi} d\varphi$$
$$= 2\pi i^{\left[\frac{\omega}{\omega_0}\right]l} J_{\left[\frac{\omega}{\omega_0}\right]l}\left(-\frac{\omega}{\omega_0}k_0 n r \sin\theta_d\right), \quad (17)$$

with $[\omega/\omega_0]$ the integer close to the value of ω/ω_0 and J the first kind of Bessel function. The fine grid integration over r from $r_i - \Delta r/2$ to $r_i + \Delta r/2$ is expressed as

$$F_2(r_i, \theta_d, \omega) = \int_{r_i - \Delta r/2}^{r_i + \Delta r/2} F_J(r, \theta_d, \omega) r \, dr. \quad (18)$$

F_2 is calculated numerically using a Gaussian-Laguerre integration, while F_1 is calculated analytically. F_1 and F_2 can be calculated separately so the three-dimensional integral reduces to just a one-dimensional integration since we assume that the laser beam is of cylindrical symmetry. Here we chose the observation direction at $\theta_d, \varphi_d = 0$ without loss of generality.

In the phase matching, we need the refractive indices (n_0, n) and the absorption coefficient Γ. The refractive index can be expressed as

$$n(\omega) = 1 + 2\pi\alpha(\omega)n_{\text{atm}} - 2\pi n_{\text{atm}}\frac{P_{\text{ion}}}{\omega^2}. \quad (19)$$

The equation is valid for a lower gas density and lower IR intensity ($< 10^{15}$W/cm^2) as shown in the experiments [49,50].

TABLE I. Polarizabilities at $\lambda = 1030$ nm for Ar, Kr, and Xe atoms used in this paper and the results of the RRPA method.

Methods	Ar	Kr	Xe
This paper	11.14	16.71	27.24
RRPA [55]	10.77	16.47	26.97
Expt. [56]	10.5	16.1	26.2

The last term stands for plasma effect due to the ionization of atoms with ionization probability P_{ion}, which is obtained when solving Eq. (5). $\Gamma(\omega)$ is the self-absorption coefficient, which relates to the photoabsorption cross section $\sigma(\omega)$ as

$$\Gamma(\omega) = \tfrac{1}{2}\sigma(\omega)n_{\text{atm}}. \quad (20)$$

The refractive index can be either found in literature or obtained by simulation.

We use $\alpha(\omega)$ and $\sigma(\omega)$ calculated by the linear-response density-functional theory with self-interaction correction [51]. The calculated cross sections are in good agreement with the experiments [52–54] for several noble gases.

To check the liability of the calculated polarizabilities by the method, we compare the polarizabilities $\alpha(\omega)$ of Ar, Kr, and Xe atoms by the method and by the relativistic random-phase approximation (RRPA), and the results are listed in Table I. The RRPA results [55] were calculated at zero frequency and the experimental data were obtained from the refractive database [56]. The simulations reasonably agree with the experiment. Therefore, we use the refractive indices and absorption coefficients calculated by Ref. [51] in this paper. We can also apply the method to other atoms.

III. RESULTS AND DISCUSSION

Since the HHG from Ar atoms has been reported recently [6,7], we use Ar as an example and choose the laser parameters close to the experiments. The parameters are the wavelength $\lambda = 1030$ nm, pulse duration $\tau = 35$ fs, and laser peak intensity $I = 2 \times 10^{14}$ W/cm^2 unless stated otherwise.

To obtain the macroscopic HHG, we first calculate the microscopic HHG at different laser intensities. Figure 2 shows the atomic HHG yield ($|d(\omega)|^2$) of Ar atoms for intensities up to 2.5×10^{14} W/cm^2. $d(\omega)$ is the Fourier transform of the dipole [Eq. (8)] in acceleration form. We also show the atomic HHGs calculated with SFA as shown in Fig. 2(b) and SFA with the Coulomb correction in Fig. 2(c). The SFA fails to describe the HHG in the lower IR intensity and the low-order HHG. Figure 2(b) shows that the SFA works well for the HHG near the cutoff for the IR intensity higher than 10^{14}W/cm^2. It can be understood that the SFA is valid for the tunneling ionization so it is not a surprise that it does not work well for a lower IR intensity. The HHG is generated when the electron returns to the parent-core so neglecting the Coulomb interaction will reduce the returning probability significantly, especially for low-energy electrons. This explains why the lower-order HHG yield is suppressed even for a higher IR intensity. For a high-energy electron, the Coulomb interaction is less important. To confirm the argument, we also calculate the HHG by adding the Coulomb correction [37] to the SFA
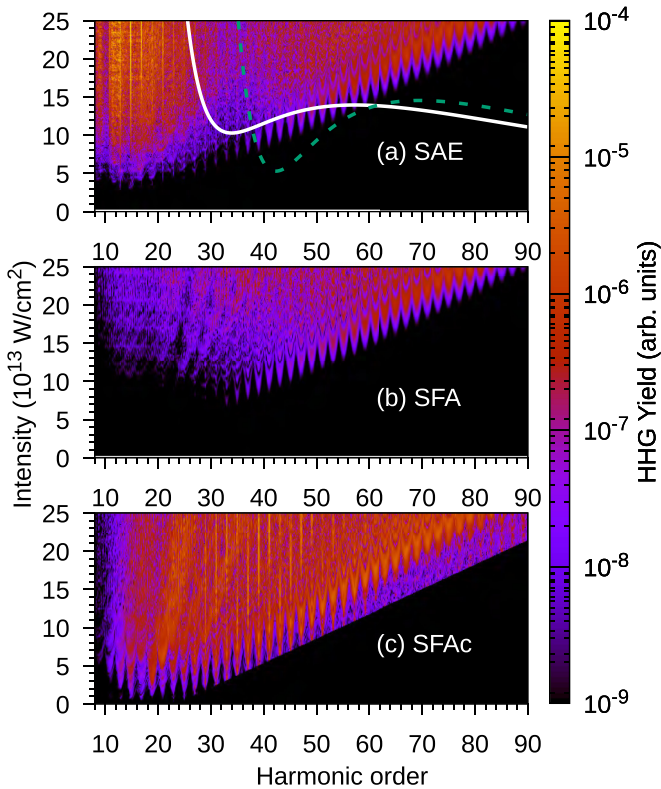
FIG. 2. Ar atomic HHG in strong laser fields with intensities up to 2.5×10^{14} W/cm^2 calculated by TDSE with (a) SAE approximation, (b) SFA, and (c) SFAc [37]. Photoionization cross sections (in the unit of 0.1 Mb) calculated with SAE using the model potential (solid line) and by linear-response theory [51] (dashed line) are also plotted in (a).

denoted as SFAc in Fig. 2(c). Indeed, with the Coulomb correction, the calculated HHG has been improved significantly, especially for the low-order HHG. The cutoffs of the HHG in the three calculations are in reasonable agreement in a broader intensity region. In Fig. 2(a), the atomic HHG has a dip structure around a harmonic order of 30, lower than the cooper-minimum position [52,57] observed in the experiment [6]. The dip does not show up in the SFA or SFAc simulation. Based on the quantitative rescattering theory [35], the dip is associated with the photoionization process. To check it, we also plot the photoionization cross sections calculated using the SAE with the model potential used to solve the TDSE (solid curve) and the one calculated by linear-response theory [51] (dashed curve) in Fig. 2(a). Indeed, the minimum of the photoionization cross section from SAE is close to the 35th HHG where the dip structures appear in the HHG obtained by TDSE with SAE. Considering the linear response, the minimum shifts to high energy at the 41st HHG which is close to the Cooper-minimum position. This explains why there is a valley around the 35th HHG in Fig. 2(a). We see clear HHG peaks near the cutoff and no clear peaks in the plateau regime.

The atomic HHG is emitted at every microscopic position, and the macroscopic HHG is the superposition of the microscopic HHG with the phase matching in Eq. (12). In the macroscopic HHG, we assume that the laser propagates along the z direction with the focus point at the origin, with beam
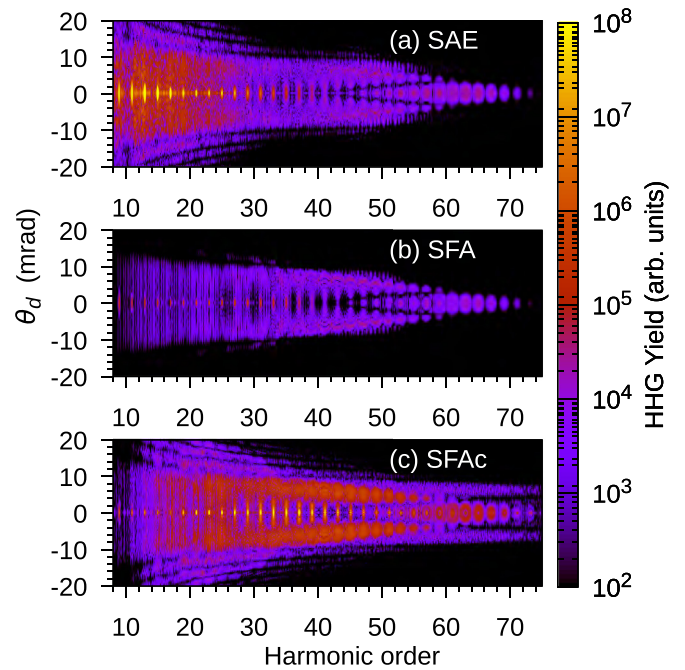

FIG. 3. Divergence of far-field HHG of Ar atoms in the strong laser field with a peak intensity of 2.0×10^{14} W/cm^2. The gas jet is located at the focal plane with gas pressure of 3.5 mbars and thickness of 1 mm using different microscopic HHGs from (a) SAE, (b) SFA, and (c) SFAc [37] in a LG00 beam as shown in Fig. 2.

waist $W_0 = 50$ μm. The media from the gas jet are on the xy plane with thickness $d = 1$ mm and the center of the plane is at z_0. The peak laser intensity 2×10^{14} W/cm^2 is picked up at the position where $S(r, z)$ in Eq. (2a) reaches its maximum. In the following, we investigate how the macroscopic HHG yield depends on the gas pressure and center position z_0.

First, we will check how the microscopic HHG affects the macroscopic HHG if we use different microscopic HHGs shown in Fig. 2. Figure 3 shows the divergence of the far-field HHG obtained with the same phase-matching procedure using different microscopic HHGs with the LG00 beam ($l = 0$, $p = 0$). The plotted macroscopic HHG is proportional to $|\boldsymbol{E}(\theta_d, \omega)|^2$ in Eq. (11). The global patterns of the macroscopic HHG are similar to each other in that there is a broader divergence about 10 mrad and strong narrow HHG peaks around $\theta_d \approx 0$. There is a node structure starting from the HHG order of $n = 40$. The global patterns, which originated from Eqs. (13b) and (13c), are essentially the same for the three simulations. The main differences of the three simulations are the HHG strengths, which originated from Eq. (13a). These observations can be explained as that the global pattern is decided by the experimental setup and phase matching, so the pattern is insensitive to the microscopic HHG. The HHG strengths depend on the microscopic HHG, and it may differ in orders from different microscopic HHGs. We conclude that the SFA can provide a qualitative macroscopic HHG, not a quantitative one.

Now, let us study the dependency of the macroscopic HHG on the different laser beam with the same IR intensity and the microscopic HHG. Figure 4 shows the macroscopic HHG for (a) a Gaussian beam or LG00 and (b) an LG10 beam
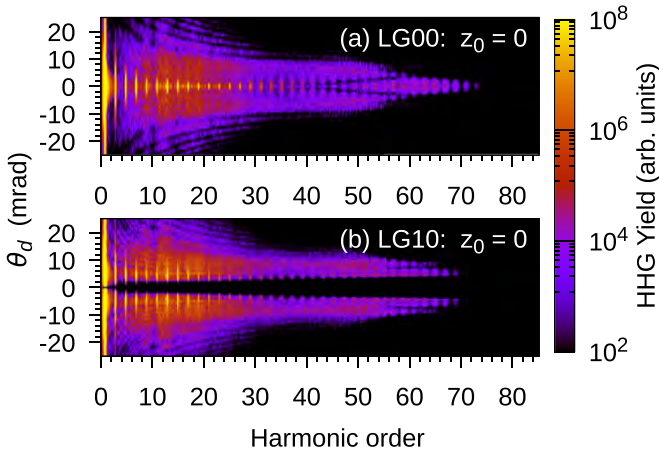
FIG. 4. Divergence of far-field HHG of Ar atoms in the strong laser field for (a) LG00 and (b) LG10 beams. All the other macroscopic parameters are the same as the ones used in Fig. 3.

FIG. 6. Divergence of far-field HHG of Ar atoms in a strong laser field at (a) $z_0 = -3$ mm and (b) $z_0 = 3$ mm for the LG00 beam. The laser parameters are the same as in Fig. 3.

($l = 1, p = 0$). For the LG10 beam, due to an additional OAM, the HHG at the center ($\theta_d = 0$) is zero. We see again that the general pattern of the macroscopic HHG is decided by the phase matching and the laser beam space distribution. Therefore, one can control the global pattern of the far-field HHG by steering the laser space distribution. For an LG10 laser beam, the HHG forms a scissor structure. The calculated divergences are in reasonable agreement with the experiment [7].

If we integrate over the divergence θ_d, we get the total emission yields ($\int (|E(\theta_d, \omega)|^2) d\theta_d$) as shown in Fig. 5. The atomic HHG is also plotted in the figure for comparison. For the single atom HHG, There are no clear harmonic structures before the cutoff. After the phase matching, clear peaks are observed for the LG00 and LG10 beams. For the lower-order HHGs below $n < 30$, the harmonic yield of LG00 is larger than the LG10. In the plateau region the HHG yield of LG10
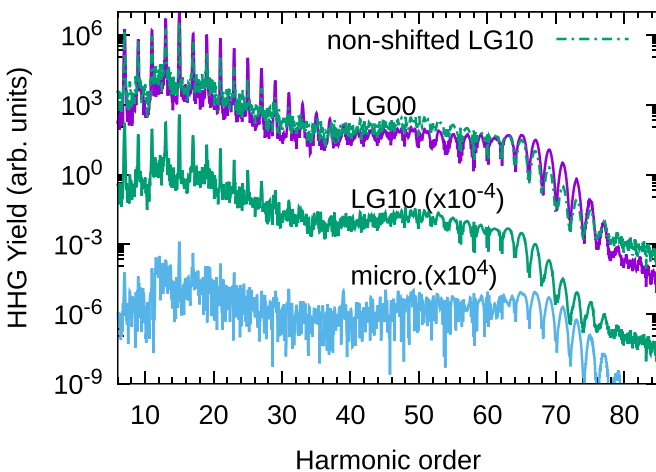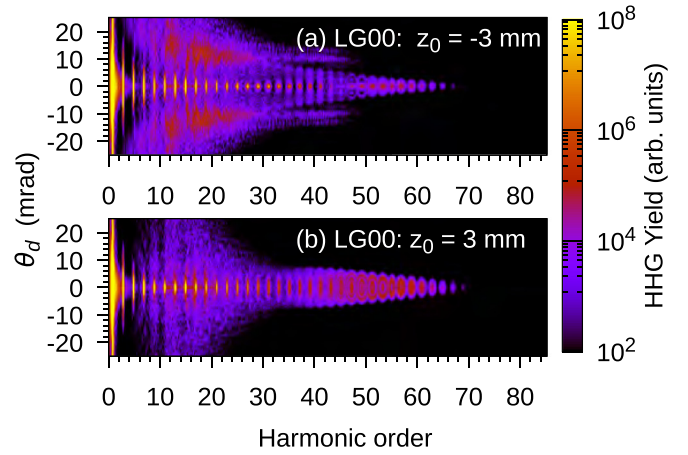

FIG. 5. Far-field HHG yields of Ar atoms in LG00 and LG10 laser beams and atomic HHG. The laser parameters are the same as in Fig. 3. The HHG from LG10 is downshifted four orders for easy comparison.

is larger than the LG00. The phase matching makes the macroscopic HHG sharper than the atomic HHG in general.

Although we marked the HHG yield in arbitrary units, the absolute values in Fig. 5 are still meaningful. The HHG from each atom is very small, many orders smaller than the macroscopic HHG. The macroscopic HHG is still strong enough for practical use.

The macroscopic HHG also depends on the gas density and gas jet position. The laser intensities on the planes at z_0 and $-z_0$ are the same due to the reflection symmetry of the LG beam, while the HHGs from the gas jet centered at z_0 and $-z_0$ are not symmetric since the phase matching breaks the symmetry. Figure 6 shows the divergence of the HHG from LG00 when the center of the gas jet is at $z_0 = -3$ and 3 mm. For $z_0 = -3$ mm, the higher-order harmonics are mainly generated at the forward side of the gas jet since the laser intensity is higher when the gas is close to the focal point as shown in Fig. 1. The higher HHGs are not dispersed further by the media, and their divergences are narrow. For $z_0 = 3$ mm, the higher-order harmonics are generated at the back side of the gas jet. They are dispersed further by the media, and the divergences are broader.

We can tune the gas pressure and gas jet position to optimize the HHG yields. Figure 7 shows the HHG yield as a function of the gas jet position and gas pressure for the 15th and 63rd HHGs. We choose the two because the 63rd HHG stands for the HHG near the cutoff and the 15th HHG stands for the HHG near the ionization threshold. If the gas pressure is too low, there are not enough atoms to generate HHGs, so the macroscopic HHG yield is low. If the gas pressure is too high, self-absorption can reduce the yield. There must be an optimal condition at which the HHG yield reaches its maximum. In Fig. 7, we see that the highest yield for the 15th HHG appears at $P = 11$ mbar$s$, $z_0 = 0.8$ mm. There are long tails at both $z_0 = -3$ and 3 mm.

For the 63rd HHG, the structure is more complex. If we pick up one gas jet position, namely, $z_0 = 0$, we see that the yield increases as the pressure increases at first, then the yield decreases as the pressure increases further. Such structure repeats as we increase the pressure continuously.
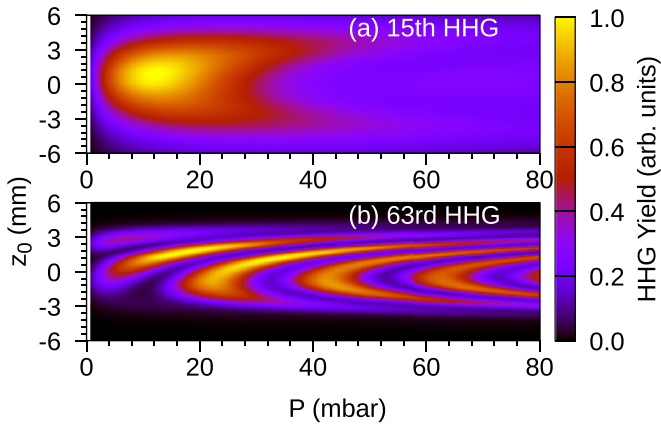
FIG. 7. Position and pressure dependency of the far-field HHG of Ar atoms in the strong LG00 laser field for (a) the 15th HHG and (b) the 63rd HHG.

The HHG yields oscillate as a function of the gas pressure. This has been observed in experiments [58,59] and attributed to the phase matching. For a given laser pulse, we can still tune the macroscopic HHG by varying the gas jet position. If the gas jet is located after the focal point, one can select the long trajectory [60–62]. For the present case, the strongest 63rd HHG appears at $P = 18$ mbars, $z_0 = 1.8$ mm. Indeed, the optimal condition depends on which HHG one wants to enhance.

In summary, we proposed a method to calculate the macroscopic high-order harmonic generation. The key steps are that we calculate the atomic HHG by directly solving the time-dependent Schrödinger equation. All the atomic phases are included without using classical trajectories. The phase matching is carried out on the nested fine and coarse grids based on physical considerations. Within the fine grid, we assume that the IR intensity does not change, and the phase associated with the propagation changes. In such a way, we calculate the macroscopic over the coarse grid with the different IR intensities and the propagation effect. Our calculated divergences of the HHG beam are in reasonable agreement with the recent experiments. Furthermore, we can tune the gas jet position and pressure to optimize a specified HHG on the macroscopic level. The method can also be used to study the HHG from multijet arrays [63]. The atomic HHG can be improved by considering electron dynamical correlation with the time-dependent density-functional theory [21,23,64].

[1] X. F. Li, A. L'Huillier, M. Ferray, L. A. Lompre, and G. Mainfray, Multiple-harmonic generation in rare gases at high laser intensity, Phys. Rev. A **39**, 5751 (1989).

[2] P. Agostini and L. F. DiMauro, The physics of attosecond light pulses, Rep. Prog. Phys. **67**, 813 (2004).

[3] F. Krausz and M. Ivanov, Attosecond physics, Rev. Mod. Phys. **81**, 163 (2009).

[4] Z. Chang, A. Rundquist, H. Wang, M. M. Murnane, and H. C. Kapteyn, Generation of Coherent Soft X Rays at 2.7 nm Using High Harmonics, Phys. Rev. Lett. **79**, 2967 (1997).

[5] T. Popmintchev, M.-C. Chen, D. Popmintchev, P. Arpin, S. Brown, S. Ališauskas, G. Andriukaitis, T. Balčiunas, O. D. Mücke, A. Pugzlys, A. Baltuška, B. Shim, S. E. Schrauth, A. Gaeta, C. Hernández-García, L. Plaja, A. Becker, A. Jaron-Becker, M. M. Murnane, and H. C. Kapteyn, Bright coherent ultrahigh harmonics in the keV x-ray regime from mid-infrared femtosecond lasers, Science **336**, 1287 (2012).

[6] G. S. Boltaev, R. A. Ganeev, N. A. Abbasi, M. Iqbal, V. V. Kim, H. Al-Harmi, X. M. Tong, and A. S. Alnaser, Routes to control cooper minimum in high order harmonics generated in argon gas, New J. Phys. **22**, 083031 (2020).

[7] M. Iqbal, G. S. Boltaev, N. Abbasi, R. A. Ganeev, and A. S. Alnaser, Spatial and spectral variations of high-order harmonics generated in noble gases, J. Phys. B **55**, 105601 (2022).

[8] O. Kfir, P. Grychtol, E. Turgut, R. Knut, D. Zusin, D. Popmintchev, T. Popmintchev, H. Nembach, J. M. Shaw, A. Fleischer, H. Kapteyn, M. Murnane, and O. Cohen, Generation of bright phase-matched circularly-polarized extreme ultraviolet high harmonics, Nat. Photonics **9**, 99 (2015).

[9] L. Allen, M. W. Beijersbergen, R. J. C. Spreeuw, and J. P. Woerdman, Orbital angular momentum of light and the transformation of Laguerre-Gaussian laser modes, Phys. Rev. A **45**, 8185 (1992).

[10] L. Allen, M. J. Padgett, and M. Babiker, *IV. The Orbital Angular Momentum of Light*, Progress in Optics Vol. 39 (Elsevier, Amsterdam, 1999), pp. 291–372.

[11] K. Y. Bliokh, F. J. Rodríguez-Fortuño, F. Nori, and A. V. Zayats, Spin-orbit interactions of light, Nat. Photonics **9**, 796 (2015).

[12] W. Paufler, B. Böning, and S. Fritzsche, Coherence control in high-order harmonic generation with Laguerre-Gaussian beams, Phys. Rev. A **100**, 013422 (2019).

[13] G. F. Quinteiro Rosen, P. I. Tamborenea, and T. Kuhn, Interplay between optical vortices and condensed matter, Rev. Mod. Phys. **94**, 035003 (2022).

[14] K. M. Dorney, L. Rego, N. J. Brooks, J. San Román, C.-T. Liao, J. L. Ellis, D. Zusin, C. Gentry, Q. L. Nguyen, J. M. Shaw, A. Picón, L. Plaja, H. C. Kapteyn, M. M. Murnane, and C. Hernández-García, Controlling the polarization and vortex charge of attosecond high-harmonic beams via simultaneous spin-orbit momentum conservation, Nat. Photonics **13**, 123 (2019).

[15] A. Baltuška, T. Udem, M. Uiberacker, M. Hentschel, E. Goulielmakis, C. Gohle, R. Holzwarth, V. S. Yakoviev, A. Scrinzi, T. W. Hansch, and F. Krausz, Attosecond control of electronic processes by intense light fields, Nature (London) **421**, 611 (2003).

[16] P. B. Corkum and F. Krausz, Attosecond science, Nat. Phys. **3**, 381 (2007).

[17] N. Shivaram, H. Timmers, X.-M. Tong, and A. Sandhu, Attosecond-Resolved Evolution of a Laser-Dressed Helium Atom: Interfering Excitation Paths and Quantum Phases, Phys. Rev. Lett. **108**, 193002 (2012).

[18] J. Feist, O. Zatsarinny, S. Nagele, R. Pazourek, J. Burgdörfer, X. Guan, K. Bartschat, and B. I. Schneider, Time delays for attosecond streaking in photoionization of neon, Phys. Rev. A **89**, 033417 (2014).

[19] S. Neppl, R. Ernstorfer, A. L. Cavalieri, C. Lemell, G. Wachter, E. Magerl, E. M. Bothschafter, M. Jobst, M. Hofstetter, U. Kleineberg, J. V. Barth, D. Menzel, J. Burgdörfer, P. Feulner, F. Krausz, and R. Kienberger, Direct observation of electron propagation and dielectric screening on the atomic length scale, Nature (London) **517**, 342 (2015).

[20] C. W. Hogle, X. M. Tong, L. Martin, M. M. Murnane, H. C. Kapteyn, and P. Ranitovic, Attosecond Coherent Control of Single and Double Photoionization in Argon, Phys. Rev. Lett. **115**, 173004 (2015).

[21] E. Runge and E. K. U. Gross, Density-Functional Theory for Time-Dependent Systems, Phys. Rev. Lett. **52**, 997 (1984).

[22] K. Nobusada and K. Yabana, High-order harmonic generation from silver clusters: Laser-frequency dependence and the screening effect of d electrons, Phys. Rev. A **70**, 043411 (2004).

[23] J. J. Carrera, Shih-I Chu, and X. M. Tong, Very-high-order harmonic generation from Ar atoms and ar$^+$ ions in super-intense pulsed laser fields: An *ab initio* self-interaction-free time-dependent density-functional approach, Phys. Rev. A **71**, 063813 (2005).

[24] D. A. Telnov, K. E. Sosnova, E. Rozenbaum, and Shih-I Chu, Exterior complex scaling method in time-dependent density-functional theory: Multiphoton ionization and high-order-harmonic generation of Ar atoms, Phys. Rev. A **87**, 053406 (2013).

[25] J. Heslar, D. A. Telnov, and Shih-I Chu, Subcycle dynamics of high-harmonic generation in valence-shell and virtual states of Ar atoms: A self-interaction-free time-dependent density-functional-theory approach, Phys. Rev. A **91**, 023420 (2015).

[26] X.-M. Tong, G. Wachter, S. A. Sato, C. Lemell, K. Yabana, and J. Burgdörfer, Application of norm-conserving pseudopotentials to intense laser-matter interactions, Phys. Rev. A **92**, 043422 (2015).

[27] M. Lewenstein, P. Balcou, M. Y. Ivanov, A. L'Huillier, and P. B. Corkum, Theory of high-harmonic generation by low-frequency laser fields, Phys. Rev. A **49**, 2117 (1994).

[28] L. Rosenberg and F. Zhou, Generalized Volkov wave functions: Application to laser-assisted scattering, Phys. Rev. A **47**, 2146 (1993).

[29] D. G. Arbó, J. E. Miraglia, M. S. Gravielle, K. Schiessl, E. Persson, and J. Burgdörfer, Coulomb-Volkov approximation for near-threshold ionization by short laser pulses, Phys. Rev. A **77**, 013401 (2008).

[30] G. Duchateau, E. Cormier, H. Bachau, and R. Gayet, Coulomb-Volkov approach of atom ionization by intense and ultrashort laser pulses, Phys. Rev. A **63**, 053411 (2001).

[31] J. Bauer, Coulomb-corrected Volkov-type solution for an electron in an intense circularly polarized laser field, J. Phys. B **34**, 1343 (2001).

[32] B. Böning and S. Fritzsche, Partial-wave representation of the strong-field approximation, Phys. Rev. A **102**, 053108 (2020).

[33] S. Fritzsche and B. Böning, Lorentz-force shifts in strong-field ionization with mid-infrared laser fields, Phys. Rev. Res. **4**, 033031 (2022).

[34] P. B. Corkum, Plasma Perspective on Strong Field Multiphoton Ionization, Phys. Rev. Lett. **71**, 1994 (1993).

[35] A.-T. Le, R. R. Lucchese, M. T. Lee, and C. D. Lin, Probing Molecular Frame Photoionization via Laser Generated High-Order Harmonics from Aligned Molecules, Phys. Rev. Lett. **102**, 203001 (2009).

[36] C. Jin and C. D. Lin, Spatially coherent high-order harmonics generated at optimal high gas pressure with high-intensity one- or two-color laser pulses, Phys. Rev. A **94**, 043804 (2016).

[37] S. V. Popruzhenko, Coulomb phase in high harmonic generation, J. Phys. B **51**, 144006 (2018).

[38] X.-M. Tong and S.-I. Chu, Theoretical study of multiple high-order harmonic generation by intense ultrashort pulsed laser fields: A new generalized pseudospectral time-dependent method, Chem. Phys. **217**, 119 (1997).

[39] E. M. Purcell and C. R. Pennypacker, Scattering and absorption of light by nonspherical dielectric grains, Astrophys. J. **186**, 705 (1973).

[40] C. Hernández-García, J. A. Pérez-Hernández, J. Ramos, E. C. Jarque, L. Roso, and L. Plaja, High-order harmonic propagation in gases within the discrete dipole approximation, Phys. Rev. A **82**, 033432 (2010).

[41] C. Jin, A.-T. Le, and C. D. Lin, Retrieval of target photorecombination cross sections from high-order harmonics generated in a macroscopic medium, Phys. Rev. A **79**, 053413 (2009).

[42] D. Wright, P. Greve, J. Fleischer, and L. Austin, Laser beam width, divergence and beam propagation factor: An international standardization approach, Opt. Quantum. Electron. **24**, S993 (1992).

[43] A. M. Yao and M. J. Padgett, Orbital angular momentum: Origins, behavior and applications, Adv. Opt. Photon. **3**, 161 (2011).

[44] W. Paufler, B. Böning, and S. Fritzsche, High harmonic generation with Laguerre-Gaussian beams, J. Opt. **21**, 094001 (2019).

[45] X. M. Tong and C. D. Lin, Empirical formula for static field ionization rates of atoms and molecules by lasers in the barrier-suppression regime, J. Phys. B **38**, 2593 (2005).

[46] X. M. Tong, K. Hino, and N. Toshima, Phase-dependent atomic ionization in few-cycle intense laser fields, Phys. Rev. A **74**, 031405(R) (2006).

[47] X. Guan, X.-M. Tong, and Shih-I Chu, Effect of electron correlation on high-order-harmonic generation of helium atoms in intense laser fields: Time-dependent generalized pseudospectral approach in hyperspherical coordinates, Phys. Rev. A **73**, 023403 (2006).

[48] J. C. Baggesen and L. B. Madsen, On the dipole, velocity and acceleration forms in high-order harmonic generation from a single atom or molecule, J. Phys. B **44**, 115601 (2011).

[49] Á. Börzsönyi, Z. Heiner, A. Kovács, M. P. Kalashnikov, and K. Osvay, Measurement of pressure dependent nonlinear refractive index of inert gases, Opt. Express **18**, 25847 (2010).

[50] J. Schwarz, P. Rambo, M. Kimmel, and B. Atherton, Measurement of nonlinear refractive index and ionization rates in air using a wavefront sensor, Opt. Express **20**, 8791 (2012).

[51] X.-M. Tong and Shih-I Chu, Density-functional theory with optimized effective potential and self-interaction correction for

ground states and autoionizing resonances, Phys. Rev. A **55**, 3406 (1997).

[52] J. R. Samson and W. C. Stolte, Precision measurements of the total photoionization cross-sections of He, Ne, Ar, Kr, and Xe, J. Electron Spectrosc. Relat. Phenom. **123**, 265 (2002).

[53] A. T. Domondon and X. M. Tong, Photoabsorption spectra of I and its ions in the $4d$ region, Phys. Rev. A **65**, 032718 (2002).

[54] T. M. Kojima, F. Chen, M. Kitajima, T. Koizumi, Y. Nakai, H. Yamaoka, and N. Watanabe, Observation of resonance structures in $4d$ photoionization of Eu+, J. Electron Spectrosc. Relat. Phenom. **144–147**, 71 (2005).

[55] W. Johnson, D. Kolb, and K.-N. Huang, Electric-dipole, quadrupole, and magnetic-dipole susceptibilities and shielding factors for closed-shell ions of the He, Ne, Ar, Ni (Cu^+), Kr, Pb, and Xe isoelectronic sequences, At. Data Nucl. Data Tables **28**, 333 (1983).

[56] A. Börzsönyi, Z. Heiner, M. P. Kalashnikov, A. P. Kovács, and K. Osvay, Dispersion measurement of inert gases and gas mixtures at 800 nm, Appl. Opt. **47**, 4856 (2008).

[57] J. W. Cooper, Photoionization from outer atomic subshells: A model study, Phys. Rev. **128**, 681 (1962).

[58] A. Rundquist III, C. G. Durfee, Z. Chang, C. Herne, S. Backus, M. M. Murnane, and H. C. Kapteyn, Phase-matched generation of coherent soft x-rays, Science **280**, 1412 (1998).

[59] O. Finke, J. Vábek, M. Nevrkla, N. Bobrova, O. Hort, M. Jurkovič, M. Albrecht, A. Jančárek, F. Catoire, S. Skupin, and J. Nejdl, Phase-matched high-order harmonic generation in pre-ionized noble gases, Sci. Rep. **12**, 7715 (2022).

[60] P. Salieres, A. L'Huillier, and M. Lewenstein, Coherence Control of High-Order Harmonics, Phys. Rev. Lett. **74**, 3776 (1995).

[61] P. Balcou, P. Sali'eres, A. L'Huillier, and M. Lewenstein, Generalized phase-matching conditions for high harmonics: The role of field-gradient forces, Phys. Rev. A **55**, 3204 (1997).

[62] Y. Mairesse, A. de Bohan, L. J. Frasinski, H. Merdji, L. C. Dinu, P. Monchicourt, P. Breger, M. Kovacev, R. Taieb, B. Carre, H. G. Muller, P. Agostini, and P. Salieres, Attosecond synchronization of high-harmonic soft x-rays, Science **302**, 1540 (2003).

[63] A. Willner, F. Tavella, M. Yeung, T. Dzelzainis, C. Kamperidis, M. Bakarezos, D. Adams, M. Schulz, R. Riedel, M. C. Hoffmann, W. Hu, J. Rossbach, M. Drescher, N. A. Papadogiannis, M. Tatarakis, B. Dromey, and M. Zepf, Coherent Control of High Harmonic Generation via Dual-Gas Multijet Arrays, Phys. Rev. Lett. **107**, 175002 (2011).

[64] I. Floss, C. Lemell, G. Wachter, V. Smejkal, S. A. Sato, X.-M. Tong, K. Yabana, and J. Burgdörfer, Ab initio multiscale simulation of high-order harmonic generation in solids, Phys. Rev. A **97**, 011401(R) (2018).